Aerosol Science and Technology
Publication details, including instructions for authors and subscription information:
http://www.informaworld.com/smpp/title~content=t713656376

Dependence of Laser-Induced Incandescence on Physical Properties of Black Carbon Aerosols: Measurements and Theoretical Interpretation

Nobuhiro Moteki[a]; Yutaka Kondo[a]
[a] Research Center for Advanced Science and Technology, University of Tokyo, Tokyo, Japan

First published on: 14 July 2010

To cite this Article Moteki, Nobuhiro and Kondo, Yutaka(2010) 'Dependence of Laser-Induced Incandescence on Physical Properties of Black Carbon Aerosols: Measurements and Theoretical Interpretation', Aerosol Science and Technology, 44: 8, 663 — 675, First published on: 14 July 2010 (iFirst)
To link to this Article: DOI: 10.1080/02786826.2010.484450
URL: http://dx.doi.org/10.1080/02786826.2010.484450

Aerosol Science and Technology, 44:663–675, 2010

ISSN: 0278-6826 print / 1521-7388 online
DOI: 10.1080/02786826.2010.484450

Dependence of Laser-Induced Incandescence on Physical Properties of Black Carbon Aerosols: Measurements and Theoretical Interpretation

Nobuhiro Moteki and Yutaka Kondo
Research Center for Advanced Science and Technology, University of Tokyo, Tokyo, Japan

We used a single-particle soot photometer (SP2) to measure the mass of individual black carbon (BC) particles down to ∼0.5 fg by means of laser-induced incandescence with an intra-cavity, continuous-wave laser. The incandescence of nine different types of BC samples was investigated to provide a physical basis for choosing appropriate BC materials for SP2 calibration. We estimated the vaporization temperatures of these BC samples from the spectral dependence of incandescence at the limit of the small size parameter x, for which spectral dependence of emissivity is known a priori. The vaporization temperatures differed by less than 2.2% among the samples. For the $x < 1$ regime of particle size, the peak amplitude of the incandescence signal measured by the SP2 was linearly proportional to the particle mass. The slopes of such linear proportionality were positively correlated with $|(m^2-1)/(m^2+2)|$, where the m is the complex refractive index of the BC particle. For particles in which $x > 1$, the rate of increase in the peak amplitude of the incandescence signal with increasing particle mass was negatively correlated with the compactness of particle shape, consistent with the theoretical prediction of emissivity, which accounts for particle shape. The incandescence–BC mass relationships were similar between fullerene soot and ambient soot sampled in Tokyo, thus suggesting that fullerene soot is a suitable calibration standard for SP2 measurements of ambient soot.

[Supplementary materials are available for this article. Go to the publisher's online edition of *Aerosol Science and Technology* to view the free supplementary files.]

1. INTRODUCTION

Black carbon (BC) or elemental carbon (EC) emitted from incomplete combustion of fossil fuels and biomass is the dominant absorber of visible-to-near-infrared radiation among atmospheric constituents in the troposphere. BC has been estimated to be an important contributor to positive radiative forcing on a global scale (Forster et al. 2007; Ramanathan and Carmichael 2008). Near hot-spot regions of BC emissions, local positive radiative forcing can be several orders of magnitude larger than the global average, changing meteorological fields such as cloud cover fraction (Feingold et al. 2005). Deposition of BC on snow or ice induces melting in early summer, thus reducing the planetary albedo (Hansen and Nazarenko 2004; Flanner et al. 2007).

The single-particle soot photometer (Model SP2) developed by Droplet Measurement Technologies, Inc. in Boulder, CO (Stephens et al. 2003; Schwarz et al. 2006; Moteki and Kondo 2007 and references therein) quantifies the mass of BC inside individual particles by means of laser-induced incandescence (LII) without interference from internally mixed semi-volatile materials or mineral dust particles. To derive the absolute BC mass per particle for ambient aerosols, the SP2 has to be calibrated with appropriate calibration standards. Thus, we need to evaluate and select appropriate BC standards for this purpose. The intensities of incandescence have been measured as a function of particle mass for various kinds of BC samples (Slowik et al. 2007; Shiraiwa et al. 2008). However, there have been no studies to date that investigate the theoretical framework of the interpretation of the relationship between the intensity of incandescence signals and the microphysical properties of BC. In this work, we provide the physical basis for the interpretation of this relationship. In our previous studies using the SP2, the ranges of measured BC mass were limited to less than ∼60 fg, corresponding to a mass equivalent diameter (d_m) of about 400 nm. This upper limit of measured BC size corresponded to the saturation threshold of signal intensity for the data-acquisition system then available for the SP2, even though ambient BC particles typically are distributed in size ranges that exceed 400 nm. Since then, we have extended the upper limit of the detectable BC size to ∼900 nm by modifying the SP2's electronics and the data-acquisition system. In this paper, we show the characteristics of incandescence for various types of BC samples measured in this extended size range, along with a theoretical interpretation based on the general theory of thermal emission. These

Received 9 January 2010; accepted 5 April 2010.
We thank Tokai Carbon Inc., Japan for providing TEM images of Tokai glassy carbon particles. This work was supported by the Ministry of Education, Culture, Sports, Science, and Technology (MEXT), the strategic international cooperative program of the Japan Science and Technology Agency (JST), and the global environment research fund of the Japanese Ministry of the Environment (B-083).
Address correspondence to Nobuhiro Moteki, Research Center for Advanced Science and Technology, University of Tokyo, 4-6-1 Komaba, Meguro-ku, Tokyo 153-8904, Japan. E-mail: moteki@atmos.rcast.u-tokyo.ac.jp

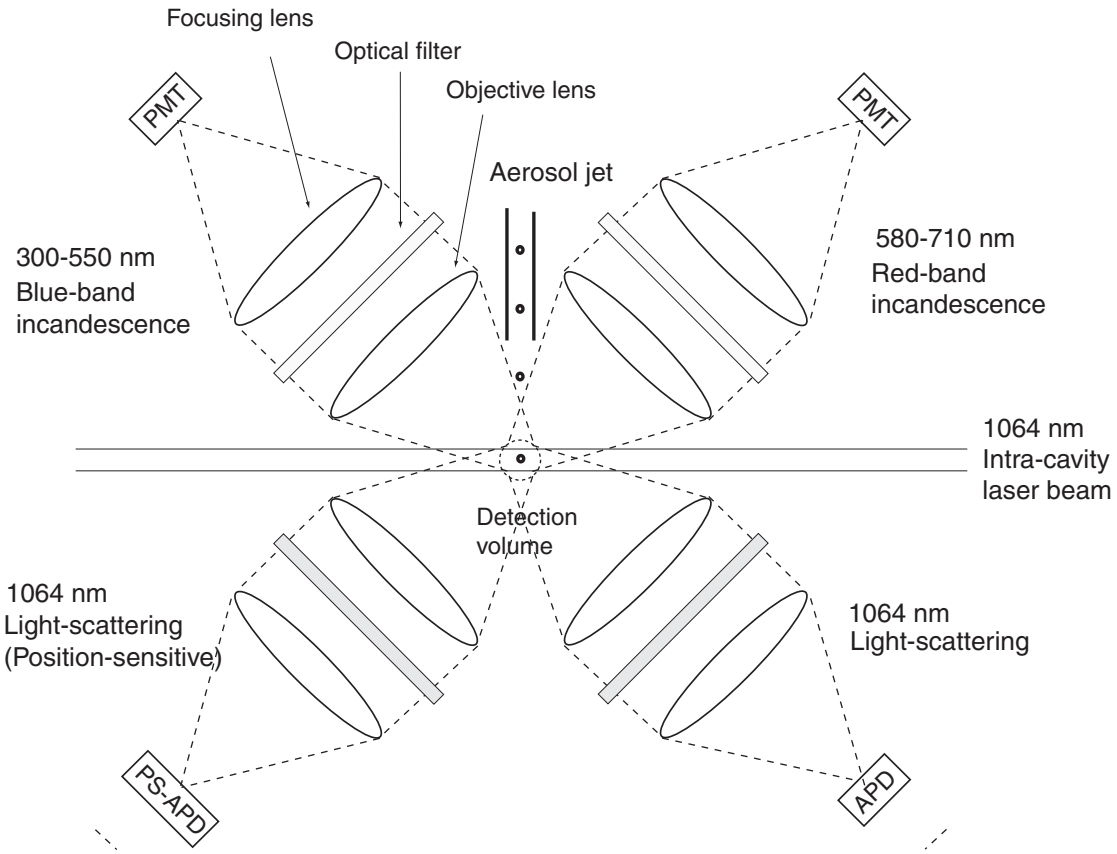

FIG. 1. Schematic diagram of the single-particle soot photometer (SP2) used in this study.

results are useful for selecting appropriate calibration standards for ambient BC measurements obtained with the SP2.

2. METHODS

2.1. Single-particle Soot Photometer (SP2)

The single-particle soot photometer (SP2) measures time-dependent scattering and incandescence signals from individual aerosol particles passing though a continuous-wave, intra-cavity Nd:YAG laser beam operating at 1064 nm (Stephens et al. 2003; Schwarz et al. 2006; Moteki and Kondo 2007; Moosmüller et al. 2009). Figure 1 shows a schematic diagram of the SP2 used in this study.

Four detection channels, each consisting of an objective lens, optical filter, focusing lens, and photo-detector, were placed symmetrically on a horizontal plane in orthogonal pairs. The direction of aerosol flow was perpendicular to the laser beam and the optical axes of the lens units. The intra-cavity laser was adjusted to TEM_{00} mode with a Gaussian intensity distribution, and the $1/e^2$ energy diameter of the laser beam at the detection volume was $\sim$1 mm. The sheath flow rate of the aerosol jet determined the speed of individual particles passing though the laser beam. The transit speed of aerosols at the detection volume was measured to be $\sim$50 m s^{-1} from the width of the Gaussian scattering waveforms. In contrast to conventional LII techniques utilizing pulsed lasers, the SP2 measures signals of a single particle rather than those of an ensemble of particles. When the relative positions of the aerosol jet and the laser beam were optimized, a particle counting efficiency close to 100% was achieved, as confirmed by a condensation particle counter (CPC 3022A, TSI Inc., USA). In this study, two of the four detection channels were utilized for detecting incandescence in two distinct visible bands: a blue-band channel for wavelengths λ = 300–550 nm, detected by a H6779 photomultiplier tube (PMT, Hamamatsu Inc., Japan); and a red-band channel (λ = 580–710 nm), detected by a H6779-02 PMT (Hamamatsu Inc.) equipped with a narrow band-pass filter (PB0640-140, Asahi Spectra Inc., Japan). Compared to the initial version of the SP2 (Stephens et al. 2003; Moteki and Kondo 2007), the sensitivity of the measured color ratio to the wavelength dependence of incandescence for the present SP2 was enhanced by increasing the contrast between the two incandescence channels. A scattering channel with a long-pass filter (Schott RG 850) and Si-avalanche photodiode (APD, C30916E, Perkin Elmer, Inc., USA) was used to monitor the scattering signal at 1064 nm (Figure 1). A second scattering channel used a position-sensitive Si-avalanche photodiode (PS-APD, C30927E-01, Perkin Elmer, Inc., USA) to estimate the position of each particle during transit through the laser beam. Position information is required to estimate the scattering

cross-section of the particle at an arbitrary position in the laser beam (Gao et al. 2007; Moteki and Kondo 2008). Moteki et al. (2010) have suggested a method to derive the refractive indices of BC particles from the scattering signals obtained by the SP2; we used these previous results to interpret the experimental results obtained in this study, as discussed in section 3.2.

We extended the upper limits of the detectable signal ranges for all detection channels by introducing multi-gain electronics and an additional fast analog-to-digital converter for simultaneous data acquisition of different gain signals for each channel. We also wrote data acquisition software associated with this hardware modification. As a result of this modification, the detectable upper limit of the incandescence signal was extended by a factor of ~13 relative to the previous configuration of the SP2, and BC particles of 0.35–800 fg mass (d_m = 70–920 nm) were detectable by the peak amplitude of the incandescence signal.

2.2. Incandescence Measurements

Here we provide the theoretical formulation of the incandescence signal measured by the SP2 in a manner more rigorous than in previous studies (Stephens et al. 2003; Moteki and Kondo 2007). This formulation provides the basis for the interpretation of experimental results shown in following sections of this report. The time-dependent intensity of the incandescence signal $S_i(t)$ measured by the SP2 can be expressed as

$$S_i(t) = \int_{\Delta\Omega}\int_{0}^{\infty} C_{emit}(v, m, \lambda, shape, \alpha, \beta, \gamma, \Omega, t) \cdot P_e(T(t), \lambda) \cdot \eta(\lambda) \cdot d\lambda d\Omega, \quad [1]$$

where C_{emit} is the emission cross-section of the thermal emission; η is a wavelength-dependent function describing the transmissivity of the optical filter and responsivity of the photodetector; Ω is the direction of radiation propagation; v is the particle volume; m is the complex refractive index; α, β, and γ are the Euler angles of particle rotation; and P_e is the Planck function in units of radiance, as described by

$$P_e(T, \lambda) = \frac{2hc^2}{\lambda^5(e^{hc/\lambda kT} - 1)}. \quad [2]$$

According to Rytov's theorem (Rytov 1953), a generalized Kirchhoff's law, the emission cross-section of an arbitrary body for radiation propagating in direction Ω is equivalent to the absorption cross-section of the same radiation propagating in the opposite direction –Ω (Rytov 1953; Moteki et al. 2009; Robitaille 2009 and references therein). Therefore, the emission cross-section in Equation (1) is defined by the absorption cross-section as

$$C_{emit}(v, m, \lambda, shape, \alpha, \beta, \gamma, \Omega, t) = C_{abs}(v, m, \lambda, shape, \alpha, \beta, \gamma, -\Omega, t). \quad [3]$$

A non-dimensional quantity, the absorption efficiency Q_{abs}, is defined by the absorption cross-section C_{abs} as

$$C_{abs}(v, m, shape, \alpha, \beta, \gamma, -\Omega, t) = \frac{\pi}{4} d_m^2 Q_{abs}(v, m, shape, \alpha, \beta, \gamma, -\Omega, t), \quad [4]$$

where d_m is the mass equivalent diameter given as

$$d_m = \left(\frac{6M}{\pi\rho_{true}}\right)^{1/3} \quad [5]$$

Here M is the particle mass and ρ_{true} is the true density of the particle considered. Equation (4) shows that the absorption efficiency Q_{abs} is defined as the absorption cross-section normalized by the geometrical cross-section of a mass-equivalent sphere. It is more convenient to use Q_{abs} instead of C_{abs} when comparing particles of different volumes. In contrast to the emissivity defined for geometrical optics approximations (Planck 1914; Robitaille 2009), Q_{abs} as defined here is the generalized emissivity, which can be applied even to objects with sizes comparable to or smaller than the wavelength of incident light. Equation (1) can be re-expressed using d_m and Q_{abs} as

$$S_i(t) = \frac{\pi}{4} d_m^2(t) \int_{\Delta\Omega}\int_{0}^{\infty} Q_{abs}(v, m, shape, \alpha, \beta, \gamma, -\Omega, t) \cdot P_e(T(t), \lambda) \cdot \eta(\lambda) \cdot d\lambda d\Omega. \quad [6]$$

As a measurable parameter for the spectral dependence of incandescence, the color ratio of the blue band to the red band is defined as

$$\frac{S_{i-blue}}{S_{i-red}}(t) = \frac{\int_{\Delta\Omega_{blue}}\int_{0}^{\infty} Q_{abs}(v, m, shape, \alpha, \beta, \lambda, -\Omega, t) \cdot P_e(T(t), \lambda) \cdot \eta_{blue}(\lambda) \cdot d\lambda d\Omega}{\int_{\Delta\Omega_{red}}\int_{0}^{\infty} Q_{abs}(v, m, shape, \alpha, \beta, \lambda, -\Omega, t) \cdot P_e(T(t), \lambda) \cdot \eta_{red}(\lambda) \cdot d\lambda d\Omega}, \quad [7]$$

where $\Delta\Omega_{blue}$ and $\Delta\Omega_{red}$ (the ranges of integration) are the solid angles of light collection for the blue-band and red-band channels, respectively. This ratio can be converted to thermodynamic temperature $T(t)$ with a priori knowledge of $Q_{abs}(t)$.

Changes in the amplitude and phase shift of thermal emission throughout the particle volume are negligibly small provided that

$$kd|m - 1| \ll 1, \quad [8]$$

where k is the wavenumber (= $2\pi/\lambda$), and d is the typical thickness of the particle body along the direction of wave propagation. Under this condition, the Rayleigh–Gans approximation (Kerker 1969; Bohren and Huffman 1983) can be used in

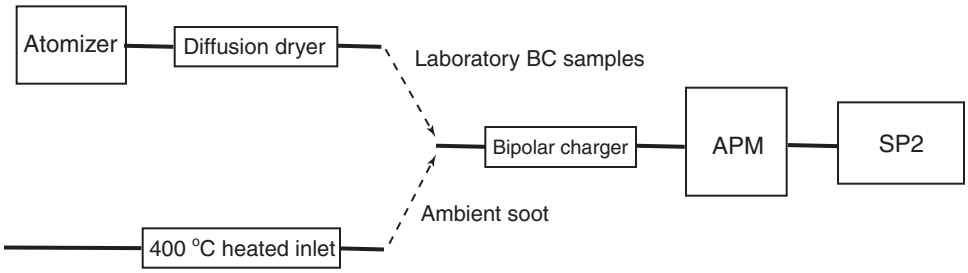

FIG. 2. Schematic diagram of the experimental setup for measurements of incandescent properties of individual BC particles of a given mass.

expressing the absorption cross-section as

$$C_{abs} = \frac{6\pi v}{\lambda} Im\left(\frac{m^2-1}{m^2+2}\right). \quad [9]$$

The corresponding absorption efficiency is expressed in terms of mass equivalent diameter as

$$Q_{abs} = \frac{4\pi d_m}{\lambda} \mathrm{Im}\left(\frac{m^2-1}{m^2+2}\right). \quad [10]$$

At the limit of the Rayleigh–Gans approximation, C_{abs} is linearly proportional to the particle volume and $\mathrm{Im}\{(m^2–1)/(m^2+2)\}$, and inversely proportional to the wavelength. Here the refractive index m is assumed to be independent of wavelength; this assumption is considered a good approximation for BC in the visible-to-near infrared wavelength region according to the available databases (Twitty and Weinman 1971; Chang and Charalampopoulos 1990; Hess et al. 1998). These formulations with the Rayleigh–Gans approximation are used to interpret the experimental data for $kd \ll 1$, as discussed in the following sections.

Under the condition of $kd \gg 1$ (i.e., the geometrical optics limit), Q_{abs} is approximated to a constant less than 1. In this regime, C_{abs} is almost exclusively determined by the geometrical cross-section of the particle because the incident light penetrating the particle's interior volume is completely absorbed near the particle surface. Therefore, the intensity of the incandescence signal is proportional to the surface area of the particle at the geometrical optics limit.

For the following discussion, we used the size parameter $x = kd_m/2$, one-half the product of wavenumber and mass-equivalent diameter, as a non-dimensional particle volume (i.e., size). When we scaled particle volume in terms of x, λ =∼500 nm was assumed to be a typical wavelength of incandescence.

2.3. Experimental Setup

Figure 2 shows the experimental setup used for measuring the incandescence properties of individual BC particles with known mass.

We used eight types of commercial laboratory BC samples and ambient soot sampled in Tokyo, Japan, as listed in Table 1. The laboratory BC samples were aerosolized from a water suspension by an atomizer and dried by a diffusion dryer with silica gel. A 400°C heated inlet (Kondo et al. 2009) was used to extract ambient soot from ambient air sampled on the campus of the Research Center of Advanced Science and Technology, University of Tokyo, located in the urban center of Tokyo. An aerosol particle mass analyzer (APM model 302, Kanomax, Japan) with a bipolar charger was used to classify masses of the BC samples prior to the SP2 measurements of incandescence. The accuracy of the mass classification was ∼3% based on measurements of standard polystyrene latex spheres (JSR Inc., Japan) with known mass. The precision of the mass classification was determined by the width of the transfer function of the APM. We developed a computer code for numerical simulations of the APM transfer function based on the theory of Ehara et al. (1996). The width of the transfer function of the APM model 302 under the operating conditions (i.e., flow rate, rotation speed, applied voltage) used in this study was less than 10% of the center mass.

3. BLACK CARBON SAMPLES

3.1. General Characteristics

Table 1 summarizes the morphological characteristics of the BC samples as measured from transmission electron microscope (TEM) images provided in previous publications.

TEM images also revealed that the morphology of the ambient soot in Tokyo was fluffy aggregates of primary spherules ∼20 nm diameter (private communication with S. Nakamura, Aoyama Gakuin University, Japan). This morphology of ambient soot is similar to that observed for diesel soot (Wentzel et al. 2003; Park et al. 2004); notably, diesel vehicles have been found to be the major source of BC in Tokyo (Kondo et al. 2006). For all these samples, BC particles were generated by means of atomization without any post-treatment, and the volume fractions of semi-volatile impurities contained in the generated BC particles were found to be negligibly small according to the time-dependent scattering cross-section data measured by the SP2 (Moteki et al. 2010).

TABLE 1
List of laboratory black carbon samples used in this study

Sample name	Information	Morphology from TEM images
Fullerene soot	Alfa Aesar Inc., Stock#40971, Lot#FS12S011	Aggregates of spherical primary particles with ~50 nm diameter, from Moteki et al. (2009).
Colloidal graphite	Alfa Aesar Inc., Stock#41773, Lot#C07M13	Aggregates of irregular flakes of graphite, from Moteki et al. (2007)
Aquadag	Acheson, USA, Ultra-fine graphite	Aggregates of irregular flakes of graphite,from Moteki et al. (2009)
Glassy carbon-100 nm(Tokai GC-100 nm)	Tokai carbon, Japan	Aggregates of spherical primary particles with ~100 nm diameter, from Figure S1 in Supplemental Information
Glassy carbon-50 nm (Tokai GC-50 nm)	Tokai carbon, Japan	Aggregates of spherical primary particles with ~50 nm diameter, from Figure S2 in Supplemental Information
Aqua-black 001	Tokai carbon, Japan	Aggregates of spherical primary particles with ~20 nm diameter, from Moteki et al. (2009)
Aqua-black 162	Tokai carbon, Japan	Aggregates of spherical primary particles with ~20 nm diameter, from Moteki et al. (2009)
Glassy carbon-0.4-12 μm(Alfa Aesar GC)	Alfa Aesar, USA, stock# 38001	Collection of spherical particles with diameters larger than ~400 nm, from Moteki et al. (2009)
Ambient soot	Sampled at Tokyo urban area, Japan	Aggregates of spherical primary particles with ~20 nm diameter, from unpublished TEM images.

3.2. Refractive Index

The $\mathrm{Im}\{(m^2-1)/(m^2+2)\}$ value is a factor that determines emissivity according to Equations (9) and (10). The $|(m^2-1)/(m^2+2)|$ values at 1064 nm for the seven types of commercial BC samples and for ambient soot were determined by Moteki et al. (2010) by simultaneous measurements of the partial scattering cross-section (ΔC_{sca}) and particle mass. We define ΔC_{sca} as the differential scattering cross-section of a particle integrated over the solid angle of light collection (Moteki and Kondo 2008; Moteki et al. 2010). As discussed by Moteki et al. (2010), 1.8 g cm^{-3} is commonly assumed to be the true density of BC samples and of ambient soot when deriving the particle volume v from

TABLE 2
Measured microphysical parameters of the BC samples used in this study

Sample name	$\lvert(m^2-1)/(m^2+2)\rvert$ values [a] from Moteki et al. (2010)	Average effective density (g cm^{-3}) for d_{mob} = 400–900 nm	Vaporization temperature (K) [b] estimated from asymptotic color ratio in $x \ll 1$ limit
Fullerene soot	0.84 (±0.04)	0.50	4230 (±30)
Colloidal graphite	1.24 (±0.31)	1.40	4230 (±30)
Aquadag	1.05 (±0.26)	0.57	4280 (±30)
Glassy carbon-100 nm (Tokai GC-100 nm)	0.81 (±0.04)	1.05	4230 (±30)
Glassy carbon-50 nm (Tokai GC-50 nm)	0.82 (±0.04)	1.27	4230 (±30)
Aqua-black 001	0.73 (±0.04)	1.05	4325 (±80)
Aqua-black 162	0.77 (±0.04)	0.85	4300 (±50)
Glassy carbon-0.4-12 μm (Alfa Aesar GC)	Not available	1.93	4260 (±10)
Ambient soot	0.78 (±0.04)	0.30	4230 (±30)

[a] ±values are the uncertainties due to the assumption for particle density that was used to derive $|(m^2-1)/(m^2+2)|$ values.
[b] ±values are the uncertainty associated with the difference in initial particle mass.

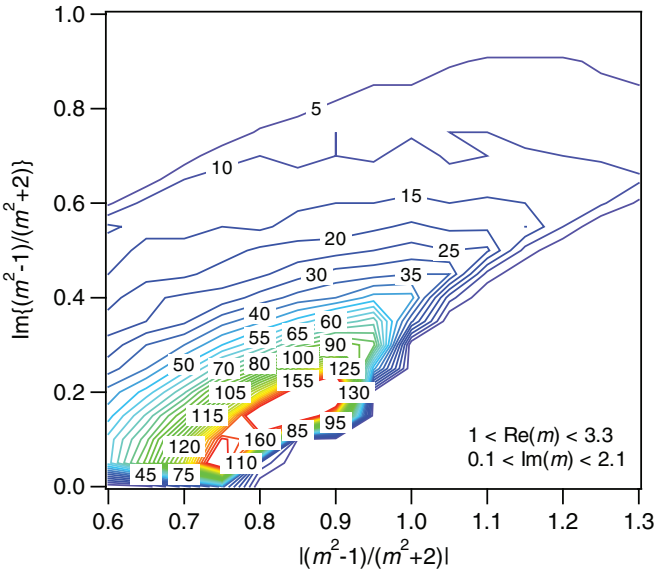

FIG. 3. Two-dimensional density distribution of $|(m^2-1)/(m^2+2)|$ and $\mathrm{Im}\{(m^2-1)/(m^2+2)\}$ mapped from homogeneously distributed two-dimensional data of $\mathrm{Re}(m)$ and $\mathrm{Im}(m)$. The considered ranges of $\mathrm{Re}(m)$ and $\mathrm{Im}(m)$ are shown in the figure. The units of density are arbitrary.

the measured particle mass, and we used this assumption in the present calculations. The $|(m^2-1)/(m^2+2)|^2$ value for each BC sample was derived from the average value of measured $\Delta C_{sca}/v^2$ for $v < 4\times10^{-21}$ m^3. Table 2 shows the determined $|(m^2-1)/(m^2+2)|$ values and their uncertainties in parentheses for each BC sample.

The uncertainty is associated with the assumption for density as discussed in Moteki et al. (2010). The $|(m^2-1)/(m^2+2)|$ values for colloidal graphite and for Aquadag were much higher than those of the other BC samples and of ambient soot. This difference in $|(m^2-1)/(m^2+2)|$ values among the samples is consistent with differences in their micro-crystalline structures observed in TEM images and electron diffraction patterns (Moteki et al. 2010). Figure 3 shows the two-dimensional density distribution of $|(m^2-1)/(m^2+2)|$ and $\mathrm{Im}\{(m^2-1)/(m^2+2)\}$ mapped from homogeneously distributed two-dimensional data of the real and imaginary parts of m, $\mathrm{Re}(m)$ and $\mathrm{Im}(m)$, respectively.

The ranges of $\mathrm{Re}(m)$ and $\mathrm{Im}(m)$ were limited to $1 < \mathrm{Re}(m) < 3.3$ and $0.1 < \mathrm{Im}(m) < 2.1$, respectively, corresponding to the ranges of reported values for BC and graphite at visible-to-near infrared wavelengths (Bond and Bergstrom 2006; Borghesi and Guizzetti 1991). Figure 3 shows a significant positive correlation of $\mathrm{Im}\{(m^2-1)/(m^2+2)\}$ with $|(m^2-1)/(m^2+2)|$ in the range of $0.7 < |(m^2-1)/(m^2+2)| < 1.3$. In the following sections, we used the measured $|(m^2-1)/(m^2+2)|$ values to interpret incandescent properties as a surrogate of $\mathrm{Im}\{(m^2-1)/(m^2+2)\}$, because there are no previously published $\mathrm{Im}\{(m^2-1)/(m^2+2)\}$ data for these BC samples.

3.3. Effective Density: An Indicator of Compactness of Particle Shape

The effective density ρ_{eff} is a parameter that describes the relationship between particle mass M and mobility diameter d_{mob} as

$$M = \frac{\pi}{6}\rho_{eff}d_{mob}^3. \quad [11]$$

The effective density is equal to the true density for spherical particles without void space. Equation (11) shows that ρ_{eff} decreases with increasing d_{mob} for fixed particle mass. As a general rule, d_{mob} positively correlates with the particle's projected area (e.g., Rogak et al. 1993), which determines the aerodynamic drag force. Therefore, ρ_{eff} increases with decreasing projected area per unit mass and can be used as an indicator of the compactness of a particle's shape.

For aerosol particles of fractal-like aggregates, the relationship between mass and mobility diameter is described by the power law as

$$M \propto d_{mob}^D. \quad [12]$$

The "mass mobility exponent" D can be used as compactness of shape of the aerosol particles (Park et al. 2004; Pagels et al. 2009). According to Equations (11) and (12), the effective density is related to Das

$$\rho_{eff} \propto d_{mob}^{D-3}. \quad [13]$$

The ρ_{eff} value for each BC sample was determined from simultaneous measurements of particle mass and mobility. We used

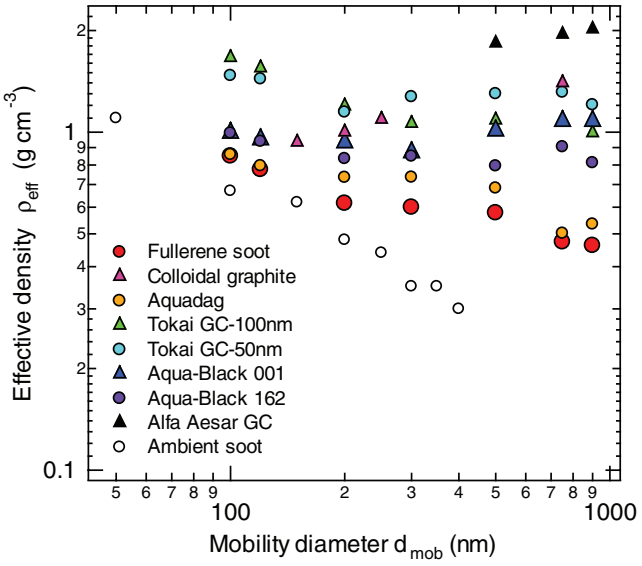

FIG. 4. Effective densities of the BC samples listed in Table 1 as a function of their mobility diameter.

the APM and a differential mobility analyzer (DMA, model 3080, TSI, Inc., USA) to measure mass and mobility, respectively. The details of the experimental setup have been described previously (Moteki and Kondo 2007). Figure 4 shows the measured ρ_{eff} as a function of d_{mob} for particle sizes of 50–900 nm.

The slope of the logarithmic plots of ρ_{eff} and d_{mob} equals $D-3$ (Equation (13)). Namely, a particle shape can be described by D provided that the slope of the data points shown in Figure 4 remains constant over the wide range of d_{mob}. The ambient soot data exhibited a constant slope over $d_{mob} = 50$–400 nm, corresponding to $D = 2.3$. This D value for ambient soot in Tokyo matches that of diesel exhaust soot ($D = 2.35$) measured by Park et al. (2004) and slightly higher than that of flame generated soot ($D = 2.15$) measured by Pagels et al. (2009). In contrast to the case of ambient soot, the slopes for the majority of the laboratory BC samples varied with d_{mob}, and their shapes could not be uniquely described by a D. The ρ_{eff} values of Tokai GC-100 nm and –50 nm and of AquaBlack 001 and 162 depended little on d_{mob}, especially for $d_{mob} > 300$ nm. The constant ρ_{eff} values independent of d_{mob} corresponded to $D = \sim 3$. This value is much higher than the reported values of $D = 2.15 \sim 2.35$ (Park et al. 2004; Pagels et al. 2009) for fresh soot samples measured directly after its generation. The much higher D of the BC samples, which were atomized from aqueous suspension, was likely due to condensation-induced restructuring (Kütz and Schmidt-Ott 1992). The Alfa Aesar-GC sample exhibited much higher ρ_{eff} values ($1.8 \sim 2$ g cm^{-3}) compared to other samples in d_{mob} range of 500–900 nm. These ρ_{eff} values are close to typical values of the reported true density ρ_{true} for BC (Bond and Bergstrom 2006; Moteki et al. 2010). This agreement of ρ_{eff} with ρ_{true} is consistent with the abundance of single spheres of 500–900 nm size in the Alfa Aesar-GC powder sample, as evidenced by TEM images (Moteki et al. 2009). Table 2 shows the average values of ρ_{eff} for the d_{mob} range of 400–900 nm for each sample. The average ρ_{eff} for $d_{mob} = 400$–900 nm represents the compactness of the particle shape in the $x > \sim 1$ regime. These data are used in interpreting the thermal emission in terms of particle shape. The effective densities of ambient soot were measured only up to $d_{mob} = 400$ nm because of very low of ambient soot concentrations at $d_{mob} > 400$ nm. Therefore, the ρ_{eff} value of ambient soot shown in Table 2 is that at $d_{mob} = 400$ nm.

4. THEORETICAL CONSIDERATIONS OF SPECTRAL EMISSIVITY

4.1. Dependence of Spectral Emissivity on Particle Geometry

First, we demonstrate the effects of particle size and shape on the particles' emissivity based on theoretical calculations. Emissivities, defined as Q_{abs} in Equation (4), were calculated for spherical particles and for fractal aggregates and are shown in Figures 5a and b, respectively.

We used Mie scattering code BHMIE (Bohren and Huffman 1983) and discrete dipole approximation code DDSCAT 7.0 (Drane and Flatau 1994; Drane and Flatau 2008) for calculations for spheres and fractal aggregates, respectively. Three-dimensional geometries of fractal aggregates were generated by the tunable particle–cluster aggregation algorithm of Filippov et al. (2000). The fractal dimension D_f for the aggregates was fixed at 2.2. The fractal aggregates of $D_f = 2.2$ was regarded as a representative of highly-branched aggregates of BC samples used in this study. The fractal prefactor, a parameter describing the stoutness of branches of fractal aggregates, was assumed to be 1. The diameter of primary spherules consisting of the aggregate was fixed at 50 nm. Given that a D_f of 2.0 is analogous to a plane, the primary spherules in fractal aggregates of $D_f = 2.2$ were not thickly shielded by other spherules. For both the spherical particles and the fractal aggregates, the wavelength dependence of Q_{abs} approached λ^{-1} for smaller particles ($M < \sim 1$ fg) as predicted by the Rayleigh–Gans approximation. For larger particles ($M > \sim 10$ fg), the wavelength dependence of Q_{abs} increased with decreasing D_f, as evident from a comparison of Figure 5a with Figure 5b. For spheres, the wavelength dependence of Q_{abs} decreased and approached a constant independent of wavelength with increasing mass (or size), as expected from geometrical optics. However, for a fractal aggregate with $D_f = 2.2$, a λ^{-1} dependence was apparent even at large particle size ($M > \sim 100$ fg), because individual primary spherules can still absorb incident light without complete shielding from other volume elements. At the theoretical limit of no shielding of incident light by other volume elements, Q_{abs} is expressed by the Rayleigh–Gans approximation. In other words, Q_{abs} is proportional to the mass equivalent diameter d_m. The effect of incomplete shielding of the fractal aggregates is evidenced by the increase in Q_{abs} with increasing particle mass as shown in Figure 5b.

4.2. Relationship Between Color Ratio and Thermodynamic Temperature

The calculated relationships between the blue-band to red-band signal ratio (i.e., the color ratio) and the thermodynamic temperature calculated from Equation (7), using the emissivities shown in Figure 5, are shown in Figures 6a and b for spheres and fractal aggregates, respectively.

We used the manufacturer's nominal values of the wavelength-dependent response of the photomultiplier tubes and the transmittance of the optical filters to determine η in Equation (7). A tungsten–halogen lamp light source with a spectral intensity distribution approximated by that of a $\sim$2800 K black body was emitted from the tip of an optical fiber within the detection volume of the particle (Figure 1), and we measured the absolute values of the relationship between the color ratio and thermodynamic temperature. This procedure ensures that the position of the light source relative to the light collection optics is the same as incandescing particles. To minimize systematic

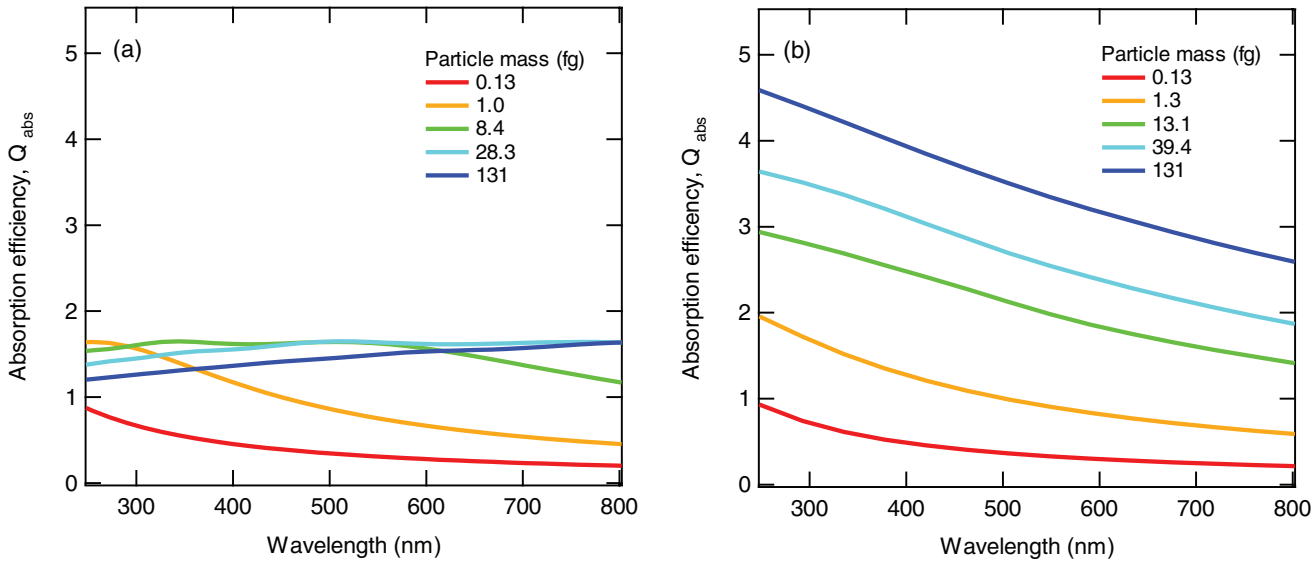

FIG. 5. Calculated wavelength-dependent absorption efficiency Q_{abs} (i.e., emissivity) for (a) spheres and (b) fractal aggregates of particles with a fractal dimension of 2.2 and primary particle diameter of 50 nm. Particle masses shown in the FIG. were calculated assuming a true density of 1.8 g cm^{-3}. The refractive index was assumed to be $m = (2.0, 0.8)$ independent of wavelength.

errors due to the inhomogeneous directional distribution of light emitted from the tip of the optical fiber, the measurements for the blue-band and red-band channels were made in the same direction of light collection and with the same objective lens unit (Figure 1). The average value of six measurements was used for scaling the relationship between the color ratio and thermodynamic temperature. The standard deviation of the color ratio for the six measurements was 5% of the average value. The thermodynamic temperature measurements based on the color ratio calculations used in this study were more accurate than previous measurements (Moteki and Kondo 2007) because the present measurements included corrections for both the possible directional dependence of light from the tip of the optical fiber and the effects of particle shape on emissivity.

Figure 6 shows that the color ratio depended both on thermodynamic temperature and particle geometry (volume and shape). For particles of sizes much smaller than the wavelength ($kd_m \ll 1$), the color ratio was nearly insensitive to particle shape and

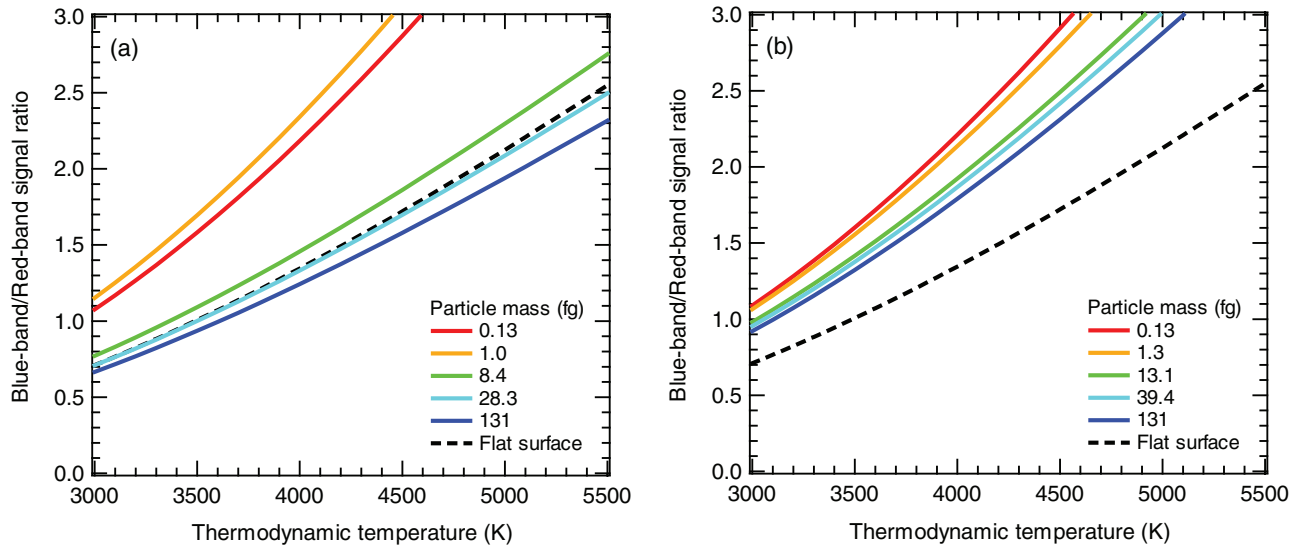

FIG. 6. Calculated blue-band/red-band incandescence signal ratios as a function of thermodynamic temperature for (a) spheres and (b) fractal aggregates, whose emissivities are shown in Figures 5a and 5b. Absolute values have been calibrated by measurements of ~2800 K black-body radiation from a tungsten–halogen lamp.

volume because of the applicability of the emissivity formula according to the Rayleigh–Gans approximation. Therefore, the thermodynamic temperature was estimated reliably from the color ratio only for particles with $kd_m \ll 1$, independent of particle shape and volume. We discuss these data further in the next section.

5. MEASUREMENT OF THE RELATIONSHIP BETWEEN INCANDESCENCE AND BC MASS

5.1. Evolution of Color Ratio in the Laser Beam

Temporal variations of the blue-band/red-band color ratio in the laser beam were measured by the SP2 for each BC sample after selection of particle mass by the APM. Figure 7 shows the average time evolutions of the color ratio for individual particles of the BC samples listed in Table 1.

Each curve represents the average values acquired from $\sim 10^3$ particles. Blue-band/red-band signal ratios were derived during the time when the signal-to-noise ratios of both channels were larger than 5. Therefore, the time duration of each plot can be interpreted as the full-width of the incandescence signal. For convenience in discussing the data, the elapsed time t was set to zero at the time of the peak amplitude of the incandescence signal for each plot in Figure 7. The steep increase in the color ratio at $t < 0$ was due to the rapid increase in thermodynamic temperature from room temperature to the vaporization temperature of BC. The steep increase stopped just before $t = 0$, when the vaporization temperature was reached. After $t = 0$, the particles shrunk due to evaporation, leading to the observed decrease in the intensity of the incandescence signal. During the evaporation after the incandescence peak (i.e., $t > 0$), the color ratio continued to increase and approached the asymptotic value $\sim$2.5 at the trailing edge of the incandescence signal (i.e., $t \sim$5–6 μs). This increase in color ratio during evaporation can be explained by the observed dependence of color ratio on particle mass (Figure 6), under the assumption that the thermodynamic temperature remained approximately the same during evaporation. Around the position of peak amplitude ($t \sim 0$), the color ratio was larger for smaller initial particle masses. This observed behavior also was consistent with the dependence of color ratio on particle mass observed in Figure 6, assuming that at $t = 0$, the vaporization temperature of each BC sample was independent of the particle mass. The vaporization temperature of BC samples can be estimated from the asymptotic value of the color ratio, which occurred at the trailing edge of the incandescence signals when d_m shrunk to be much smaller than λ (i.e., $x \ll 1$), because the λ^{-1} dependence of Q_{abs} given by Equation (10) can be applied independent of particle shape and volume. We have no experimental report on the time-dependent temperature of particles during continuous evaporation in the SP2 laser beam. Therefore, at present we use the particle temperature derived at the $x \ll 1$ limit as a representative vaporization temperature for the BC samples. The color-ratio asymptotic value of $\sim$2.5 corresponded to a thermodynamic temperature of $\sim$4250 K, according to the relationships shown in Figure 6. The vaporization temperatures of the BC samples estimated by this procedure are summarized in Table 2. The precision in the vaporization temperature is shown by the $\pm$ notation taking into account the variation of asymptotic color ratios according to different initial particle masses. The accuracy of the vaporization temperature is dependent on the accuracy of the nominal values used for the calculation of the curves in Figure 6; these values were provided by the equipment manufacturers for the wavelength-dependent properties of the tungsten–halogen lamp, optical filters, and PMTs. The possibility for the introduction of systematic errors owing to use of these nominal values was prevalent among all measurements in this study. Therefore, a possible systematic error in vaporization temperature should not have affected the relative differences in incandescent properties among the BC samples. As summarized in Table 2, the systematic differences in vaporization temperature among all BC samples and ambient soot were only 2.2%. A 2.2% variation in vaporization temperature is estimated to cause 9% difference in the signal intensity, assuming an approximately fourth-power dependence of incandescence signal intensity on particle temperature.

5.2. Relationships Between Peak Incandescence Signal and Particle Mass

In practice, the peak amplitude of the incandescence signal is the most appropriate parameter for quantifying BC mass because the peak signal contains information on BC before it is significantly evaporated in the laser beam, as discussed in section 5.1. We investigated the relationships between the peak amplitude of the incandescence signal and particle mass separately in two mass regimes: $x < \sim 1$ ($M < 10$ fg) and $x > \sim 1$ ($20 < M < 800$ fg).

5.2.1. $x < \sim 1$ regime

In the small-volume regime of $x <\sim 1$, C_{abs} can be approximated by Equation (9) independent of shape. Therefore, in this regime, the controlling factors of incandescence can be quantified without influence from uncertainties associated with unknown particle shapes. Figure 8a shows the relationship between the peak amplitude of the blue-band incandescence signal and particle mass in the $x < \sim 1$ regime ($M < 10$ fg) for the various BC samples and for ambient soot.

For each BC sample, the peak amplitude was proportional to mass and all data points were well-fitted by a line passing through the origin. The slopes of the fitted lines varied from $\sim$49 for Aqua-Black 001 to $\sim$76 for colloidal graphite. These slopes showed no significant positive correlation with the vaporization temperatures shown in Table 2, thus demonstrating that differences in the vaporization temperature contributed little to variations in the slope. Instead, Equation (10) combined with Equation (6) (Rayleigh–Gans approximation) predicts that the slope is proportional to $\mathrm{Im}\{(m^2-1)/(m^2+2)\}$. Therefore, we plotted the correlation between the slopes and the values of $|(m^2-1)/(m^2+2)|$ from Table 2 (Figure 8b).

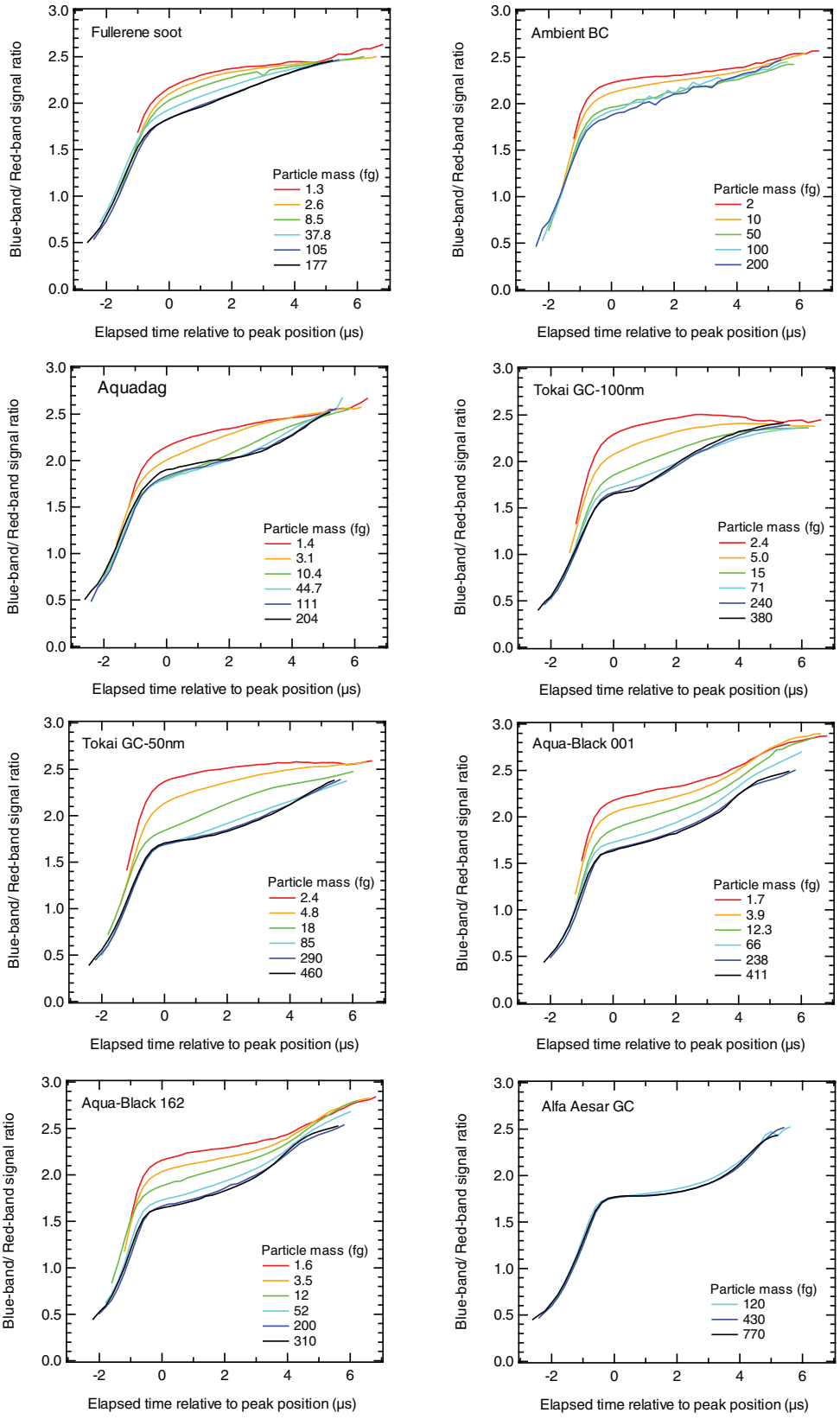

FIG. 7. Measured temporal changes of the blue-band/red-band incandescence signal ratio for various BC samples. Time $t = 0$ was fixed to correspond to the peak position of the incandescence signal for each sample. (Figure provided in color online.)

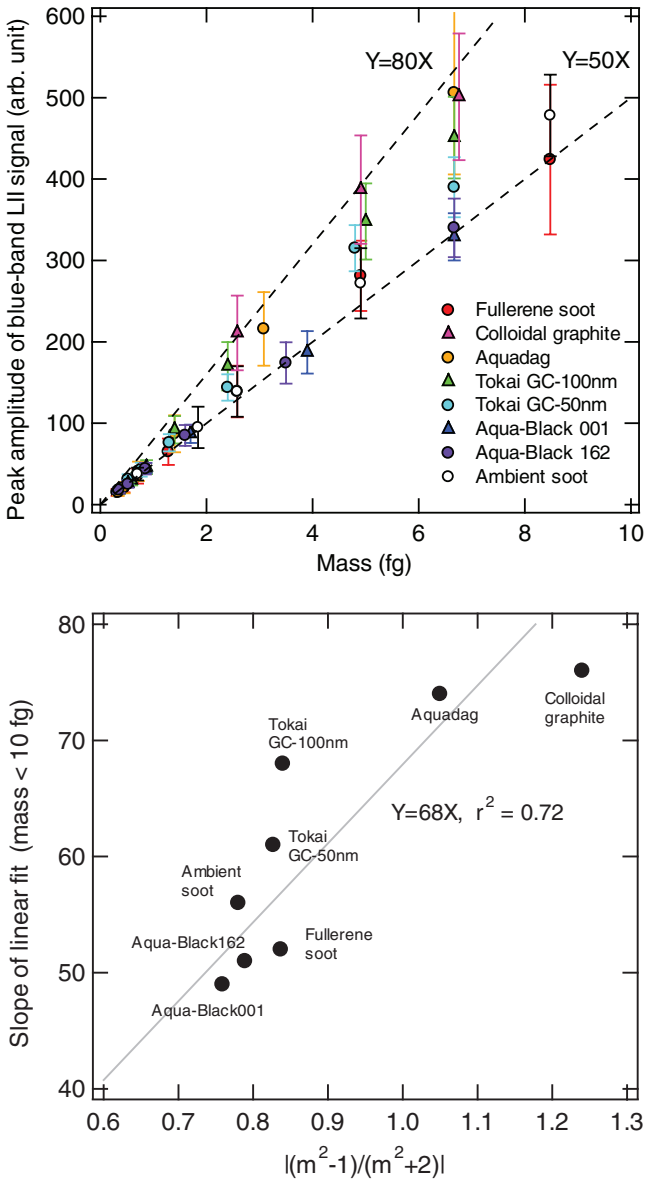

FIG. 8. (a) Measured relationship between peak amplitude of the blue-band incandescence signal and particle mass for particle masses less than 10 fg. Each data point and error bar indicates the average and standard deviation for $\sim 10^3$ particles. Reference lines with approximately maximum and minimum slope values are shown as a broken line. (b) Relationship between the slopes of the linear fits for the data in Figure 8a and $|(m^2-1)/(m^2+2)|$ values from Table 2, where m is the complex refractive index.

This data set was fitted by a line with zero offset and a correlation coefficient $r^2 = 0.72$. We interpreted this positive correlation by the Rayleigh–Gans approximation, for which the incandescent intensity is proportional to $\mathrm{Im}\{(m^2-1)/(m^2+2)\}$, because $\mathrm{Im}\{(m^2-1)/(m^2+2)\}$ was positively correlated with $|(m^2-1)/(m^2+2)|$ in the range of the measured $|(m^2-1)/(m^2+2)|$ values (i.e., 0.7–1.24) as shown in Figure 3. This analysis demonstrates that the differences in the incandescence–mass relationships among the different types of BC in the $x < \sim 1$ regime are likely due to the differences in the samples' refractive indices.

5.2.2. $x > \sim 1$ regime

Figure 9a shows the experimental results for particle masses up to 800 fg.

In this $x > \sim 1$ regime, peak amplitudes of the incandescence signal were considerably lower than the values predicted from extrapolated lines from the $x < \sim 1$ regime (i.e., slopes

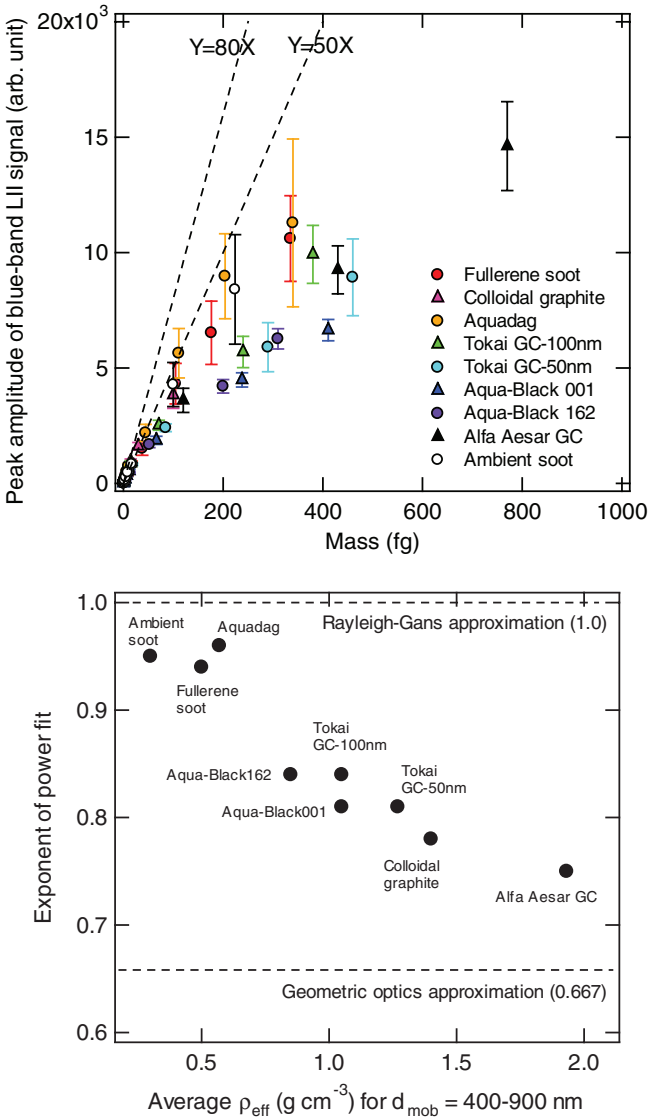

FIG. 9. (a)Measured relationship between peak amplitude of the blue-band incandescence signal and particle mass for particle masses up to 800 fg. Each data point and error bar indicates the average and standard deviation for $\sim 10^3$ particles. The reference lines shown in Figure 8a are also shown in this figure. (b) Relationship between the exponent of the power fit for the data in Figure 9a and the average effective density of BC samples for mobility diameters in the range of 400–900 nm. The theoretical limits according to the Rayleigh-Gans approximation and the geometrical optics approximation are also shown as dashed lines.

of 50–80). In the $x > \sim 1$ regime, particle shape becomes a dominant factor determining the spectral emissivity of thermal emission, as discussed in section 4.1. Theoretically, even in the $x > \sim 1$ regime, the Rayleigh–Gans approximation can still be applied to particles with extremely non-compact shapes, because each volume element that is not completely shielded can directly interact with incident radiation. In contrast, particles with extremely compact shapes (i.e., sphere, cube) follow the prediction by the geometrical optics approximation at the limit of $x \gg \sim 1$. The experimental data shown in Figure 9a were fitted by a power function of the form $y = ax^b$, where a and b are the least-squares fitting parameters. These parameters were more strongly controlled by the data points in the larger mass regime, because the horizontal distance between the neighboring data points increases with increasing particle mass. Therefore, the parameter b is expected to approach unity for particles of extremely non-compact shape (Rayleigh–Gans approximation), whereas b approaches 2/3 (= 0.667) for particles of extremely compact shapes (geometrical optics approximation). The fitted b values varied between those expected at the two extremes of non-compact and compact shapes, from ~0.75 for spherical GC (Alfa Aesar) to ~0.95 for Aquadag and ambient soot, which were fluffy aggregates of thin flakes and small spherules. Figure 9b shows the correlation between the parameter b and the average ρ_{eff} values shown in Table 2 for d_{mob} = 400–900 nm.

ρ_{eff} is a measure of the compactness of the particle shape, which can vary from zero for extremely non-compact particles up to the true density (~1.8 g cm^{-3}) for extremely compact particles. The negative correlation shown in Figure 9b demonstrates the validity of our interpretation of the difference in incandescence peak amplitudes in terms of the particles' shapes.

6. IMPLICATION FOR SP2 CALIBRATION

As demonstrated in section 5, for BC particles smaller than the wavelength of incident light (i.e., for cases of $x < 1$), the refractive index is likely an important factor of concern for SP2 calibration. In contrast, for particles larger than the wavelength ($x > 1$), particle shape becomes the dominant factor of concern for SP2 calibration. For ambient soot measurements, it is necessary to choose a calibration material whose refractive index and particle shape are close to those of ambient soot. At least for ambient soot in Tokyo urban area, the fullerene soot is the best choice among the eight commercial BC samples tested here, considering the similarities of the physical properties shown in Figures 8b and 9b. Further investigations on the refractive indices and particle shapes of other laboratory BC samples and ambient soot in other environments are necessary to improve the accuracy of BC mass (volume) measurements by the SP2.

7. CONCLUSION

To provide a physical basis for SP2 calibration for ambient BC measurements, we have investigated the relationships between the characteristics of incandescence and microphysical properties for eight types of commercial BC samples as well as for ambient soot sampled from Tokyo, Japan. The vaporization temperatures of the eight commercial BC samples and of ambient soot were found to differ by less than 2.2%, according the analysis of the time evolutions of the color ratios of incandescence in the SP2 laser beam for each sample. In the $x < \sim 1$ regime, the measured peak amplitude of incandescence was linearly proportional to the particle mass. The slopes of such correlations were positively correlated with $|(m^2\text{-}1)/(m^2\text{+}2)|$ values, which were measured independently from the analysis of light scattering data (Moteki et al. 2010). This correlation also was consistent with the emissivity predicted by Rayleigh–Gans theory, considering that $|(m^2\text{–}1)/(m^2\text{+}2)|$ was positively correlated with $\mathrm{Im}((m^2\text{–}1)/(m^2\text{+}2))$ for the range of measured $|(m^2\text{–}1)/(m^2\text{+}2)|$ values.

In the $x > \sim 1$ regime, the peak amplitude of incandescence is predicted to be proportional to particle mass (volume) for particles with extremely non-compact shapes, whereas the peak amplitude should be proportional to 2/3 (0.667) of the particle's mass (volume) for particles with extremely compact shapes. Consistent with this theoretical prediction, the rates of the increase in the peak amplitude with the increasing particle mass were negatively correlated with the particles' effective density. The present experimental measurements, combined with the theoretical calculations, clearly demonstrate the importance of accounting for the refractive index in the $x < \sim 1$ regime and for particle shape in the $x > \sim 1$ regime when selecting appropriate BC calibration standards for ambient BC measurements by the SP2. The observed incandescence–BC mass relationships were similar between fullerene soot and ambient soot sampled in Tokyo. Although further investigation is needed on the refractive indices and particle shapes of other laboratory BC samples and on ambient soot in other environments, at this point, the current results support the use of fullerene soot as a calibration standard for SP2 measurements of ambient soot.

REFERENCES

Bohren, C. F., and Huffman, D. R. (1983). *Absorption and Scattering of Light by Small Particles*, John Wiley & Sons, Inc.

Bond, T. C., and Bergstrom, R. W. (2006). Light Absorption by Carbonaceous Particles: An Investigative Review. *Aerosol Sci. Technol.* 40:27–67.

Borghesi, A., and Guizzetti, G. (1991). Graphite (C), in *Handbook of Optical Constants of Solids II*, E. D. Palik, ed., Academic Press, New York, p. 449.

Chang, H., and Charalampopoulos, T. T. (1990). Determination of the Wavelength Dependence of Refractive Indices of Flame Soot, *Proc. Royal Society London A*, 430, 577–591.

Draine, B. T., and Flatau, P. J. (1994). Discrete-Dipole Approximation for Scattering Calculations. *J. Optical Society of America A*, 11, 1491–1499.

Draine, B. T., and Flatau, P. J. (2008). *Users Guide for the Discrete Dipole Approximation Code DDSCAT 7.0*, http://arxiv.org/abs/0809.0337v4.

Ehara, K., Hagwood, C., and Coakley, K. J. (1996). Novel Method to Classify Aerosol Particles According to Their Mass-to-Charge Ratio-Aerosol Particle Mass Analyzer, *J. Aerosol Sci.* 27:217–234.

Feingold, G. H., Jiang, H., and Harrington, J. Y. (2005). On Smoke Suppression of Clouds in Amazonia, *Geophys. Res. Lett.* doi:10.1029/2004GL021369.

Filippov, A. V., Zurita, M., and Rosner D. E. (2000). Fractal–Like Aggregates: Relation Between Morphology and Physical Properties, *J. Colloid and Interface Sci.* 229:261–273.

Flanner, M. G., Zender, C. S., Randerson, J. T., and Rasch, P. J. (2007). Present–Day Climate Forcing and Response from Black Carbon in Snow, *J. Geophys. Res.*, 112:D11202, doi:10.1029/2006JD008003.

Forster, P., V. Ramaswamy, P. Artaxo, T. Berntsen, R. Betts, D. W. Fahey, J. Haywood, J. Lean, D. C. Lowe, G. Myhre, J. Nganga, R. Prinn, G. Raga, M. Schulz, and R. Van Dorland (2007). *Changes in Atmos. Constituents and in Radiative Forcing*. In: *Climate Change 2007: The Physical Sci. Basis. Contribution of Working Group I to the Fourth Assessment Report of the Intergovernmental Panel on Climate Change,* Solomon, S., D. Qin, M. Manning, Z. Chen, M. Marquis, K. B. Averyt, M. Tignor, and H. L. Miller (eds.), Cambridge University Press, New York.

Gao, R. S., Schwarz, J. P., Kelly, K. K., Fahey, D. W., Watts, L. A., Thompson, T. L. et al. (2007). A Novel Method for Estimating Light–Scattering Properties of Soot Aerosols using a Modified Single–Particle Soot Photometer. *Aerosol Sci. Technol.* 41:125–135.

Hansen, J., and Nazarenko, L. (2004). Soot Climate Forcing via Snow and Ice Albedos, *Proc. Natl. Ac. Sci.* 101, 423–428.

Hess, M., Koepke, P., and Schult, I. (1998). Optical Properties of Aerosols and clouds: The Software Package OPAC. *Bulletin of the American Meteorological Society*, 79:831–844.

Janzen, J. (1979). The Refractive Index of Colloidal Carbon. *J. Colloid and Interface Sci.* 69:436–447.

Kerker, M. (1969). *The Scattering of Light and Other Electromagnetic Radiation*. Academic, New York.

Kondo, Y., Komazaki, Y., Miyazaki, Y., Moteki, N., Takegawa, N., Kodama, D., Deguchi, S., Nogami, M., Fukuda, M., Miyakawa, T., Morino, Y., Koike, M., Sakurai, H., and Ehara, K. (2006). Temporal Variations of Elemental Carbon in Tokyo. *J. Geophys. Res.,* 111, D12205, doi:10.1029/2005JD006257.

Kondo Y., Sahu, L., Kuwata, M., Miyazaki, Y., Takegawa, N., Moteki, N., Imaru, J, Han, S., Nakayama, T., Kim Oanh, N.T., Hu, M., Kim, Y. J., and Kita, K. (2009). Stabilization of the Filter–Based Absorption Photometry by the use of a Heated Inlet. *Aerosol Sci. Technol.* 43:741–756.

Kütz, S., and Schmidt-Ott, A. (1992). Characterization of Agglomerates by Condensation–Induced Restructuring, *J. Aerosol Sci.* 23:S357–S360.

Moosmüller, H., Chakrabarty, R. K., and Arnott, W. P. (2009). Aerosol Light Absorption and its Measurements: A Review, *J. Quant. Spectros. Radiat. Trans.* 110:844–878.

Moteki, N., and Kondo, Y. (2007). Effects of Mixing State of Black Carbon Measurement by Laser–Induced Incandescence. *Aerosol Sci. Technol.* 41:398–417.

Moteki, N., and Kondo, Y. (2008). Method to Measure Time–Dependent Scattering Cross Sections of Particles Evaporating in a Laser Beam. *J. Aerosol Sci.* 39:348–364.

Moteki, N., Kondo, Y., Takegawa, N., and Nakamura, S. (2009). Directional Dependence of Thermal Emission from Nonspherical Carbon Particles, *J. Aerosol Sci.* 40:790–801.

Moteki, N., Kondo, Y., and Nakamura, S. (2010). Method to Measure Refractive Indices of Small Nonspherical Particles: Application to Black Carbon Particles, *J. Aerosol Sci.* doi:10.1016/j.jaerosci.2010.02.013.

Pagels, J., Khalizov, A. F., McMurry, P. H., and Zhang, R. Y. (2009). Processing of Soot by Controlled Sulphuric Acid and Water Condensation~ Mass and Mobility Relationship. *Aerosol Sci. Technol.* 43: 629–640.

Park, K., Kittelson, D. B., and McMurry, P. H. (2004). Structural Properties of Diesel Exhaust Particles Measured by Transmission Electron Microscopy (TEM): Relationships to Particle Mass and Mobility. *Aerosol Sci. Technol.* 38, 881–889.

Planck, M. (1914). *The Theory of Heat Radiation*. English Translation by Masius, M., P. Blakiston's Son & Co.

Ramanathan, V., and Carmichael, G. (2008). Global and Regional Climate Changes Due to Black Carbon. *Nature Geo. Sci.* 1, 221–227.

Robitaille, P.-M. (2009). Kirchhoff's Law of Thermal Emission: 150 Years. *Progress in Physics*, 4:3–13.

Rogak, S. N., Flagan, R. C., and Nguyen, H. V. (1993). The Mobility and Structure of Aerosol Agglomerates. *Aerosol Sci. Technol*. 18: 25–47.

Rytov, S. (1953). *The Theory of Electrical Fluctuations and Thermal Radiation*, U.S.S.R. Academy of Science, Moscow. English transl. by U.S. Air Force Cambridge Research Center, Bedford, Massachusetts, Rep. AFCRC–TR–59–162.

Schwarz, J. P., Gao, R. S., Fahey, D. W., Thomson, D. S., Watts, L. A., Wilson, J. C., Reeves, J. M., Darbeheshti, M., Baumgardner, D. G., Kok, G. L., Chung, S. H., Schulz, M., Hendricks, J., Lauer, A., Kärcher, B., Slowik, J. G., Rosenlof, K. H., Thompson, T. L., Langford, A. O., Loewenstein, M., and Aikin, K. C.(2006). Single-Particle Measurement of Mid Latitude Black Carbon and Light-Scattering Aerosols from the Boundary Layer to the Lower Stratosphere. *J. Geophys. Res.* 111, D16207, doi:10.1029/2006JD007076.

Shiraiwa, M., Kondo, Y., Moteki, N., Takegawa, N., Sahu, L. K., Takami, A., Hatakeyama, S., Yonemura, S., and Blake, D. R. (2008). Radiative Impact of Mixing State of Black Carbon Aerosol in Asian Outflow. *J. Geophys. Res.* 113, D24210, doi:10.1029/2008JD010546.

Slowik, J. G., Cross, E. S., Han, J.-H., Davidovits, P., Onasch, T. B., Jayne, J. T., Williams, L. R., Canagaratna, M. R., Worsnop, D. R., Chakrabarty, R. K., Moosmüller, H., Arnott, W. P., Schwarz, J. P., Gao, R.-S., Fahey, D. W., Kok, G. L., and Petzold, A. (2007). An Inter-Comparison of Instruments Measuring Black Carbon Content of Soot Particles. *Aerosol Sci. Technol.* 41: 295–314.

Stephens, M., Turner, N., and Sandberg, J. (2003). Particle Identification by Laser-Induced Incandescence in a Solid-State Laser Cavity. *Appl. Opt.* 42:3726–3736.

Twitty, J. T., and Weinman, J. A. (1971). Radiative Properties of Carbonaceous Aerosols. *J. Appl. Meteorol.* 10:725–731.

Wentzel, M., Gorzawski, H., Naumann, K.-H., Saathoff, H., and Weinbruch, S. (2003). Transmission Electron Microscopical and Aerosol Dynamical Characterization of Soot Aerosols. *J. Aerosol Sci.* 34:1347–1370.